

Article

Highly Efficient RGO-Supported Pd Catalyst for Low Temperature Hydrocarbon Oxidation

Ralitsa Velinova , Anton Naydenov , Diana Kichukova, Ventsislav Tumbalev, Genoveva Atanasova , Daniela Kovacheva *  and Ivanka Spassova 

Institute of General and Inorganic Chemistry, Bulgarian Academy of Sciences, 1113 Sofia, Bulgaria

* Correspondence: didka@svr.igic.bas.bg

Abstract: The work presents Pd-containing catalysts for practical application with enhanced low-temperature activity in the complete oxidation of volatile organic compounds (VOCs) using innovative combinations of reduced graphene oxide (RGO) and alumina. The catalysts were characterized by XRD, SEM, TEM, XPS, low-temperature N₂-adsorption, and CO chemisorption. The tests on complete catalytic oxidation of different VOC (propane, butane, hexane, dimethyl ether, toluene, propylene) and CO were carried out. The reaction kinetics and the mechanism of the reaction of complete oxidation of toluene are being investigated in detail. The results show that the new catalyst design makes it able to completely oxidize the studied VOCs and CO at low temperatures (100–350 °C) with long-term stability. Using a variety of instrumental methods, it was established that for high activity and long-term stability, the optimal ratio Pd/PdO should be close to 1:1. The most probable mechanism of complete toluene oxidation is the mechanism of Langmuir–Hinshelwood. The high activity and the weak effect of water on the catalyst performance leads to further perspectives for the application of the currently developed approach for the preparation of large-scale monolithic catalytic systems for air pollution control.

Keywords: complete VOCs oxidation; RGO; palladium; kinetics of toluene oxidation; mechanism



Citation: Velinova, R.; Naydenov, A.; Kichukova, D.; Tumbalev, V.; Atanasova, G.; Kovacheva, D.; Spassova, I. Highly Efficient RGO-Supported Pd Catalyst for Low Temperature Hydrocarbon Oxidation. *Catalysts* **2023**, *13*, 1224. <https://doi.org/10.3390/catal13081224>

Academic Editor: Hongxing Dai

Received: 12 July 2023

Revised: 17 August 2023

Accepted: 18 August 2023

Published: 20 August 2023



Copyright: © 2023 by the authors. Licensee MDPI, Basel, Switzerland. This article is an open access article distributed under the terms and conditions of the Creative Commons Attribution (CC BY) license (<https://creativecommons.org/licenses/by/4.0/>).

1. Introduction

Volatile organic compounds (VOCs) are among the main air pollutants, which are precursors to the formation of ozone in the ground layer of the atmosphere and, along with fine dust particles, are the main cause of the formation of photochemical smog [1]. This causes serious damage to human health and has a harmful effect on vegetation. Two main approaches for VOCs elimination have been proposed and accepted in practice: the first one is capturing (sorption, separation) and the second one is transformation (degradation, catalytic oxidation). The first mode is suitable for the purification of VOCs with high concentrations and is hindered by perplexing processes accompanied by high costs [2–4]. Among the technologies applied for their elimination, the catalytic oxidation to carbon dioxide and water has been considered the most beneficial and efficient due to high efficiency and low process temperatures [5,6]. This technique can be applied for the elimination of VOCs with low concentrations.

Among the catalysts used for VOCs oxidation, two main groups can be outlined. The first group comprises noble metals such as platinum, palladium, gold, ruthenium, or rhodium [7–9]. Their thermal stability and catalytic activity are high, but their use is limited by their high cost and some operational restrictions (sensitivity in humid media). The second group contains a large number of individual and mixed transition metal oxides [10–12]. The advantage is their low cost and abundance; however, their activity is, in general, lower than those of the representatives in the first group. Significant achievements have been obtained by using Pd as a catalyst for the elimination of VOCs. Due to its specific electron configuration and high chemical stability [13], Pd is found to be the most attractive

for the industrial application of VOCs oxidation among the noble metals [14–18]. Many authors claimed that the catalytic behaviour of Pd-based catalysts depends on the loading quantity and oxidation state of Pd [19], its mean particle size and distribution [20–22], and on the physical and chemical properties of the supports.

For practical applications, both groups of catalysts are combined with different supports in order to enhance the number of catalytic active centres. Numerous natural or synthetic inorganic compounds were used as catalytic supports (alumina, silica, zirconia, zeolites, ceramics, etc.). High catalytic functionality is usually achieved by fine combination and synergy of the chemical properties of the active phase and the support, accounting for the possible interaction between them [23,24]. As a result of such interactions, the electronic structure of the active phase can be significantly rearranged, which reflects in the performance of supported catalysts. A well-pronounced support effect is found for Pd-based catalysts because their activity is tightly related to the type of support materials.

Unfortunately, the presence of water vapours in the gas mixture (or formed in the entire reaction) can deactivate many of the hydrophilic catalytic systems in VOCs oxidation over Pd-based catalysts. Moreover, some authors pointed out that sulphur compounds in the emitted gases also led to the deactivation of Pd catalysts [25,26].

The nature of the catalytic support strongly affects the catalytic activity of Pd-based catalysts in wet media [27,28]. The formation of hydroxyl groups on the catalyst's surface (in particular, in the case of alumina support) in the presence of water vapor is considered to block the interaction of the target gas molecules with the PdO sites, resulting in the inhibition of the catalytic reaction [29,30]. It should be noted that water vapor inhibits stronger reactions at lower temperatures [31]. To decrease this inhibition effect, some authors proposed the use of hydrophobic types of support [32].

Hydrophobic activated carbon supports have been successfully applied for low-temperature complete oxidation of VOCs [31,33]. Additionally, carbonaceous materials provide a large specific surface area, total pore volume, presence of micropores and surface functional groups [34–36]. A comparative study has shown the advantages of the carbon nanofiber (CNF) over the γ -Al₂O₃ as a support of Pt and Pd catalysts for benzene, toluene, and m-xylene oxidation due to the more hydrophobic nature of the CNF surface [36]. The reason is that the hydrophobicity of the support surface hinders the adsorption of the water molecules, which are blocking the active centres; therefore, they prevent the deactivation of the catalyst. In contrast, the adsorption of organic compounds over the catalyst surface is facilitated by the hydrophobic nature of the support [37]. However, carbonaceous supports show some deficiencies when used at higher temperatures in oxygen-rich gas streams. It will be very beneficial to combine the advantages of hydrophobic carbon material with the high stability of alumina support.

The aim of this work is to prepare Pd-containing catalysts with enhanced low-temperature activity for the complete oxidation of volatile organic compounds using innovative combinations of reduced graphene oxide (RGO) and alumina.

2. Results and Discussion

2.1. Scanning Electron Microscopy

A SEM photograph of RGO (Figure 1a) shows the typical sheet-like morphology of the reduced graphene oxide. In contrast, the RGO–Al composite (Figure 1d) shows that graphene sheets are coated with alumina phase. Finely dispersed Pd-containing particles can be seen on the SEM photographs of both Pd/RGO and Pd/RGO–Al (Figure 1b,e). The EDS spectra of the Pd/RGO and Pd/RGO–Al show the presence of 8 wt. % Pd for Pd/RGO (Figure 1c) and 1.6 wt. % for Pd/RGO–Al, respectively (Figure 1f).

2.2. Low-Temperature Nitrogen Adsorption

Low-temperature nitrogen adsorption was performed to evaluate the texture parameters of the studied samples. The adsorption–desorption isotherms of RGO, RGO-alumina composite, and catalysts Pd/RGO, Pd/RGO–Al are presented in Figure 2; the pore size

distributions are shown as insets in the same Figure. The texture parameters of the above samples are placed in Table 1. The pure RGO exhibits isotherm of II–IV type with H3 hysteresis, indicating slit-shaped pore formation between the graphene sheets [38]. The deposition of palladium does not significantly change the morphology of the support RGO because the type of isotherms and hysteresis are preserved, but the deposition leads to redistribution of the porous space and seems to predominantly proceed in the micropores. The adsorption isotherms of both composite RGO–Al and Pd/RGO–Al are of IV type according to the IUPAC classification with H1 type hysteresis, evidencing mesoporous materials with well-defined cylindrical-like pores. It could be seen that the deposition of the palladium has a slight influence on the porous structure, probably due to the very small amount of the palladium applied.

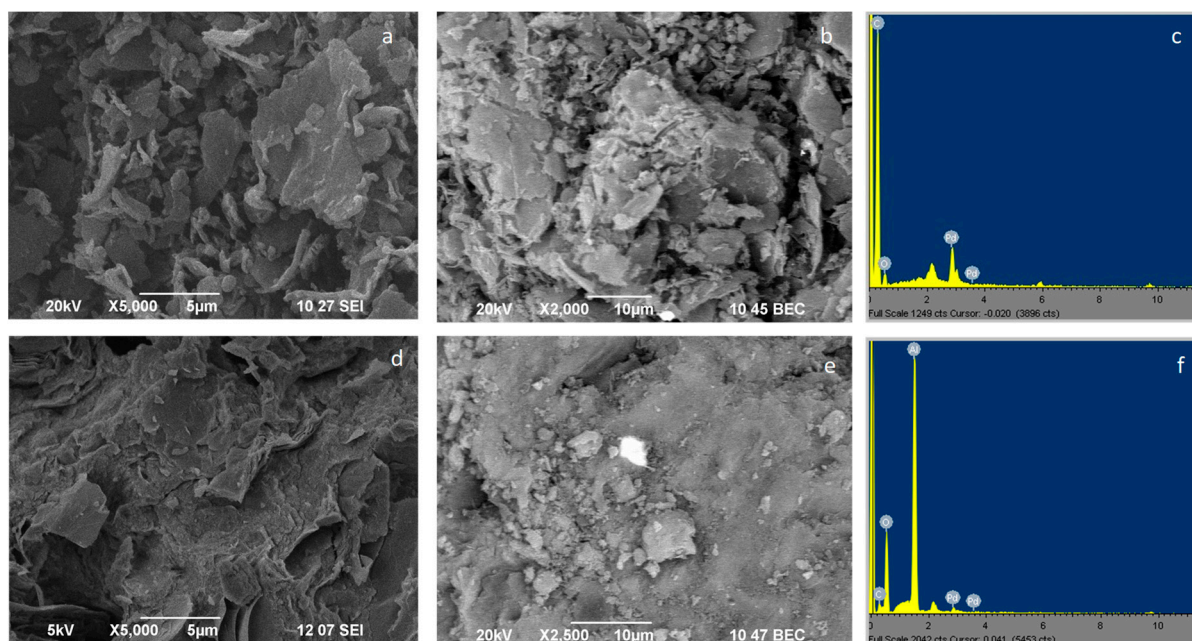


Figure 1. SEM images of: (a) RGO; (b) Pd/RGO; (c) EDS of Pd/RGO; (d) RGO–Al; (e) Pd/RGO–Al; (f) EDS of Pd/RGO–Al.

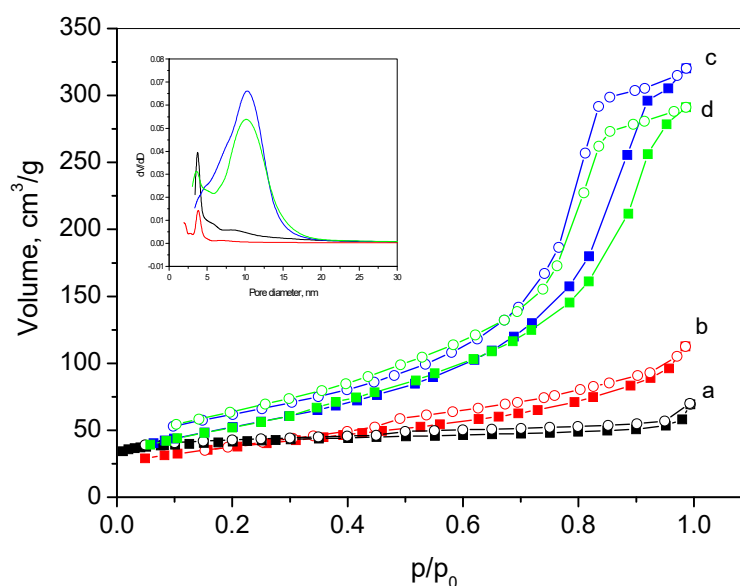


Figure 2. Nitrogen adsorption–desorption isotherms and pore size distributions of (a) RGO; (b) Pd/RGO; (c) RGO–Al; (d) Pd/RGO–Al. Full symbols: adsorption, empty symbols: desorption.

Table 1. Texture characteristics of RGO, Pd/RGO, RGO-Al, Pd/RGO-Al.

Sample	S ¹ m ² /g	V ² cm ³ /g	D _{av} ³ nm	S _{mi} ⁴ m ² /g	S _{ext} ⁴ m ² /g	V _{mi} ⁴ cm ³ /g
RGO	158	0.11	2.7	123	35	0.05
Pd/RGO	134	0.17	5.2	28	106	0.01
RGO-Al	191	0.50	10.0	-	191	-
Pd/RGO-Al	189	0.47	9.5	-	189	-

¹ BET; ² at p/p₀ ≈ 0.99; ³ NLDFT; ⁴ V-t method. The values of all calculated parameters (according to the Rouquerol criteria) have a standard error of ±2%.

2.3. Powder X-ray Diffraction

XRD patterns of RGO as well as fresh and used catalysts (Pd/RGO-Al and ES-Pd/RGO/Al/c) are presented in Figure 3; some parameters derived from XRD patterns are summarized in Table 2. The analyses of XRD patterns reveal that for Pd/RGO-Al, the palladium phase is highly dispersed and cannot be detected in the XRD patterns. A significant difference in the RGO and γ-Al₂O₃ crystallite sizes and structure was not detected between the fresh and used catalysts. In contrast, the ES-Pd/RGO/Al/c XRD provide evidence for the successful loading of palladium on the RGO support, forming mainly PdO with traces of metallic Pd. For this catalyst, after the catalytic tests, the amount of metallic Pd increases, accompanied by a more significant increase in its crystallite size.

Table 2. Phase composition, unit cell parameters, and main coherent domain size for the RGO, fresh, and spent complex catalysts. Combined data from XRD, SAED, and HRTEM.

Sample	RGO	PdO (XRD)	PdO (TEM) PDF#41-1107	Pd (XRD)	Pd (TEM) PDF#46-1043	γ-Al ₂ O ₃
RGO	100% 13 nm P63/mmc a = 2.447 Å c = 6.676 Å	-	-	-	-	-
Pd/RGO-Al fresh	5% 12 nm P63/mmc a = 2.478 Å c = 6.725 Å	Not detected <2 nm	(112)-1.70 Å	Not detected <2 nm	(200)-1.98 Å	95% 6 nm Fd-3 m a = 7.919 Å
Pd/RGO-Al used	5% 12 nm P63/mmc a = 2.455 Å c = 6.767 Å	Not detected <2 nm	(110)-2.16 Å	Not detected <2 nm	(200)-1.97 Å	95% 6 nm Fd-3 m a = 7.932 Å
ES-Pd/RGO/Al/c fresh	87% 22 nm P63/mmc a = 2.455 Å c = 6.705 Å	12.5% 10 nm P42/mmc a = 3.040 Å c = 5.308 Å	(002)-2.70 Å (110)-2.17 Å (112)-1.69 Å (211)-1.30 Å	0.5% 21 nm Fm-3 m a = 3.885 Å	(311)-1.17 Å (222)-1.10 Å	Traces
ES-Pd/RGO/Al/c used	90% 25 nm P63/mmc a = 2.457 Å c = 6.714 Å	8%, 15 nm P42/mmc a = 3.038 Å c = 5.315 Å	(002)-2.69 Å (110)-2.15 Å (112)-1.70 Å (103)-1.55 Å (004)-1.35 Å	2%, 38 nm Fm-3 m a = 3.886 Å	(200)-1.98 Å (220)-1.40 Å (311)-1.20 Å	Traces

2.4. Transmission Electron Microscopy

TEM images at different magnifications, high-resolution TEM (HRTEM) images, and selected area electron diffraction (SAED) patterns for Pd/RGO-Al and ES-Pd/RGO/Al/c catalysts (fresh and after the catalytic tests) are arranged in Figure 4. The obtained HRTEM and SAED values for the inter-planar distances of identified phases are presented in Table 2.

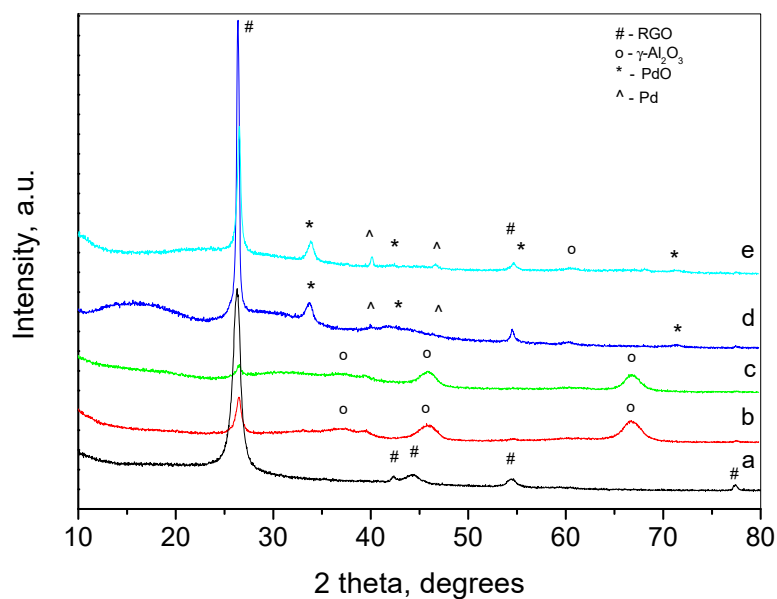


Figure 3. XRD patterns of: (a) RGO; (b) Pd/RGO–Al fresh; (c) Pd/RGO–Al used; (d) ES-Pd/RGO/Al/c fresh; (e) ES-Pd/RGO/Al/c used.

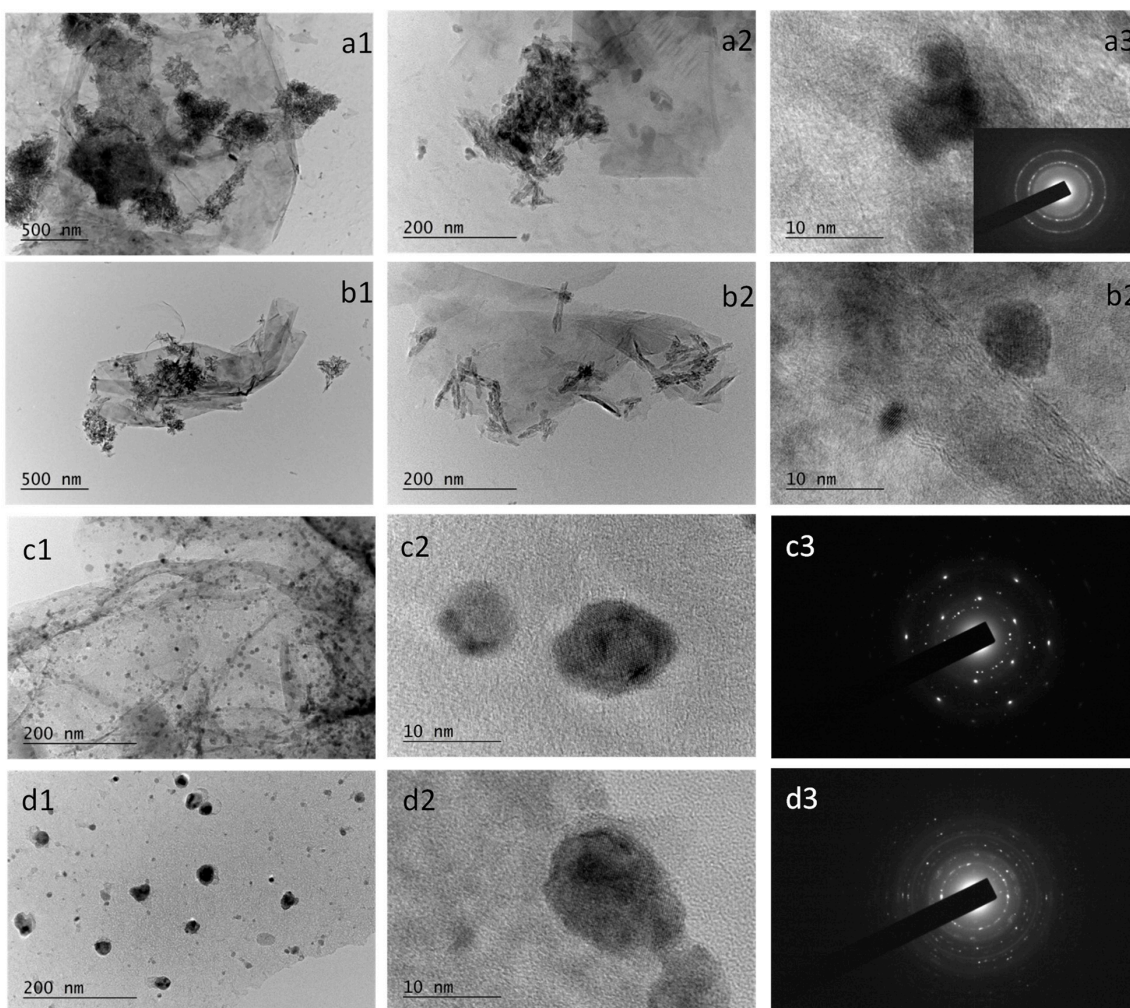


Figure 4. Bright field micrographs at different magnifications, HRTEM and SAED of: (a) Pd/RGO–Al fresh; (b) Pd/RGO–Al used; (c) ES-Pd/RGO/Al/c fresh; (d) ES-Pd/RGO/Al/c used.

The images shown in Figure 4 (a1,2,b1,2) confirm the SEM observation that alumina wraps the RGO sheets. Palladium-containing particles (PdO and Pd) that were not seen in the XRD patterns appear to have a size of about 3–4 nm (Figure 4(a3)), while larger particles appeared in the HRTEM images of the used Pd/RGO–Al catalyst (Figure 4(b3)). Very homogeneously spread Pd-containing particles on the RGO sheets can be seen on the TEM image of the fresh ES-Pd/RGO/Al/c (Figure 4(c1,2)). Figure 4(d1,2) shows that after the catalytic tests, part of the Pd-containing particles became larger in size, while some particles remained at the initial sizes. Such an increase in particle size is related to the partial reduction of PdO and the formation of metallic Pd. This observation is in good agreement with XRD results (See Table 2). No substantial change in the morphology of RGO could be seen after catalysis.

2.5. X-ray Photoelectron Spectroscopy

XPS was applied for the analysis of the surface state of the deposited palladium for both types (Pd/RGO–Al and ES-Pd/RGO/Al/c) of fresh and used catalysts. For the estimation of the oxidation state, peak deconvolution was made. The Pd 3d region of the spectra is presented in Figure 5. For all samples, Pd 3d_{5/2} peak is situated at 337.4 eV, which corresponds to Pd²⁺ [39]. A peak with binding energy 335.4 eV is attributed to Pd⁰ (metallic Pd) [40]. In all cases, the Pd 3d_{3/2} peaks are also presented (with a separation of ~5.3 eV) due to the spin-orbital splitting [41]. Despite the fact that Pd-containing phases were not seen in the XRD patterns, the XPS spectra of Pd 3d of Pd/RGO–Al (fresh and used, see Figure 5a,b) indicate the presence of palladium on the catalyst's surface. In both cases, the two oxidation states of palladium are observed with 2:1 predomination of Pd⁰ over Pd²⁺ content (Pd⁰—69.2%, Pd²⁺—30.8%). A slight change in palladium oxidation state (reduction) is registered after the catalytic tests (Pd⁰—72.0%, Pd²⁺—28.0%). In contrast, the XPS spectrum of the fresh ES-Pd/RGO/Al/c (Figure 5c) consists mainly of Pd²⁺ (Pd⁰—14.3%, Pd²⁺—85.7%). After the catalytic test, a significant change in the oxidation state of palladium can be observed. A reduction of PdO to metallic Pd resulted in almost equal quantities of the two kinds of surface palladium species (Pd⁰—51.8%, Pd²⁺—48.2%) (Figure 5d). These results completely coincide with those, which are found in XRD and TEM analyses.

2.6. Catalytic Tests of Pd/RGO–Al

For the needs of the catalytic tests, the material obtained from the hydrothermal synthesis Pd/RGO–Al was crashed and sieved to obtain a 0.3–0.6 mm fraction. The GHSV maintained for this catalyst was 100,000 h^{−1}. The steady-state conversion of CO and several VOCs as a function of a temperature was measured for the catalyst Pd/RGO–Al in air, and the results are shown in Figure 6.

As can be seen, the oxidation of CO proceeds at the lowest temperatures where the complete oxidation was achieved at 140 °C. The data from the tests of the VOCs (except propane) show that they are oxidized completely at relatively low temperatures 150–350 °C, with the lowest values for T₅₀ being observed for propylene. It is worth mentioning that for all VOCs, a complete oxidation to CO₂ and H₂O was detected. The complete oxidation of tested n-alkanes proceeds at slightly higher temperatures than the oxidation of other VOCs tested due to the peculiarities of physicochemical characteristics of molecules of VOCs, such as structure type, the strength of adsorption, ionization potential, etc. [42]. As can be expected, the most difficult to oxidize among the tested compounds is propane, and the increase in the reaction temperature of hexane through butane to propane oxidation correlates well with the C–H bond strength of the n-alkanes studied [43,44].

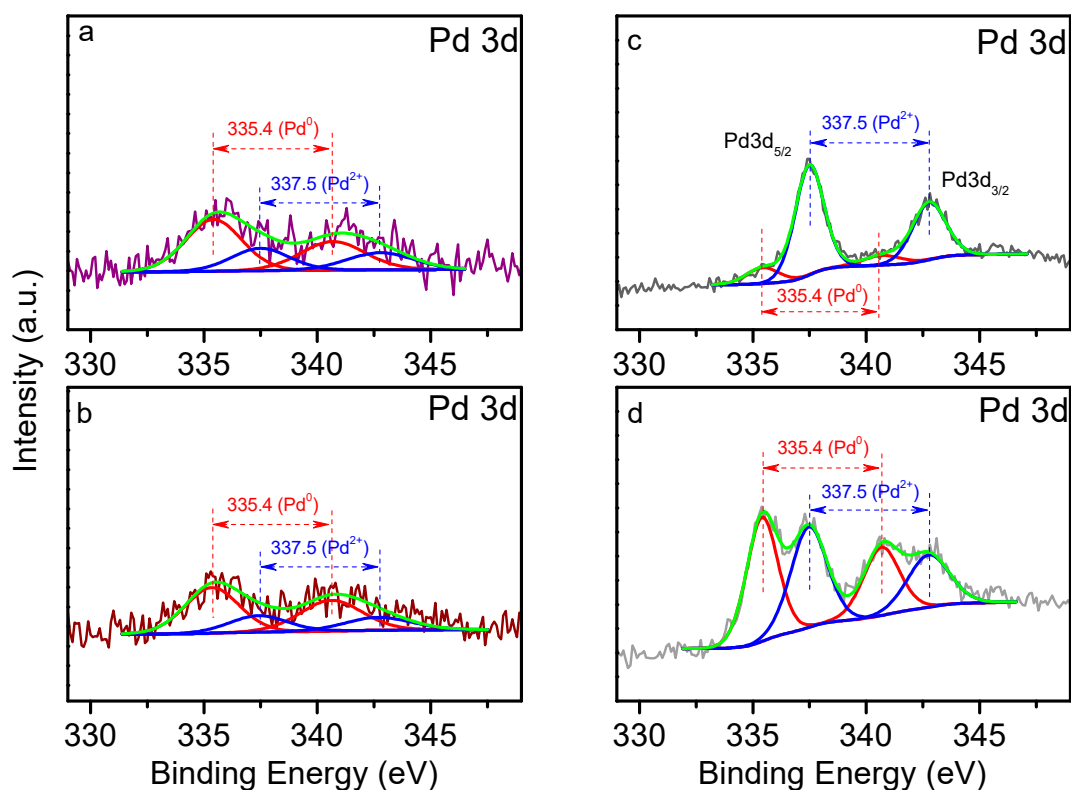


Figure 5. Pd 3d spectra of: (a) Pd/RGO–Al fresh; (b) Pd/RGO–Al used; (c) ES-Pd/RGO/Al/c fresh; (d) ES-Pd/RGO/Al/c used.

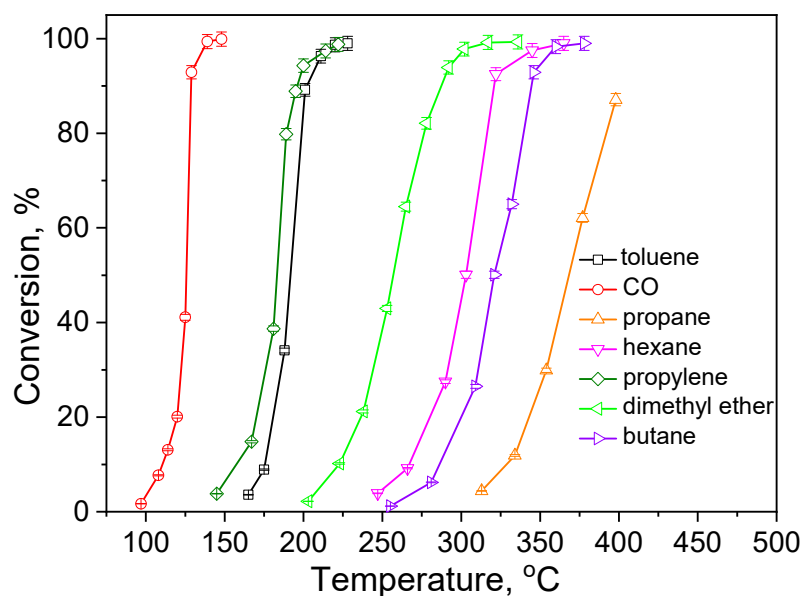


Figure 6. Temperature dependencies of the VOCs and CO conversion on Pd/RGO–Al catalyst.

2.7. Catalytic Tests of ES-Pd/RGO/Al/c

The practical application of any catalyst for VOCs oxidation rises specific requirements for the catalyst design: granulometric distribution, thermal and mechanical sustainability, long-term activity, and stability. For this purpose, the second type of catalyst (ES) was tested for the same VOCs oxidation and the results are presented in Figure 7.

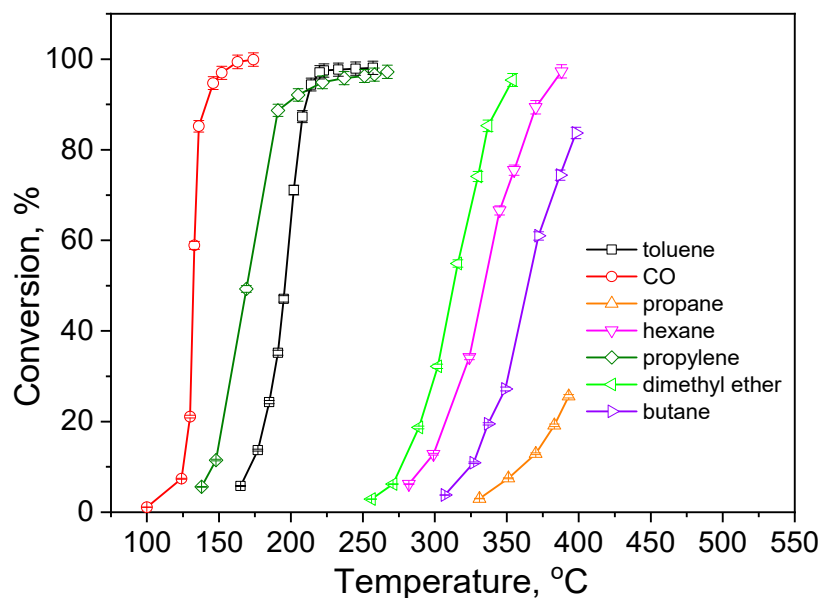


Figure 7. Temperature dependencies of the VOCs and CO conversion on ES-Pd/RGO/Al/c supported catalyst.

The comparison of the T_{50} for the different VOCs on the two catalyst designs (Figures 6 and 7) shows that temperatures are in similar ranges for CO, propylene, and toluene; however, within the case of dimethyl ether, hexane, butane, and propane, temperatures are 30–40 °C higher for the ES-Pd/RGO/Al/c catalyst. It should be pointed out that the ES-Pd/RGO/Al/c catalyst maintained its initial activity during 200 h with no signs of probable decrease in activity both in the presence or absence of additional water vapour in the gas feed. The catalysts practically do not show a deactivation during all the stability and activity tests.

2.8. CO Chemisorption on ES-Pd/RGO/Al/c

In order to quantify the exposed Pd sites on the surface of the catalyst ES-Pd/RGO/Al/c, CO chemisorption experiments were carried out. The obtained data (Figure S1) show an active metal surface of 1.10 m²/g on the active phase, or 0.06 m²/g of the total catalyst sample (the active phase supported in the form of a thin layer on the catalytic carrier with a thickness of 50 µm). For comparison, the experiment at 0 °C showed an active metal surface of 0.053 m²/g per total catalyst amount. The amount of the surface Pd atoms is 3.5% of the total amount of Pd supported on the catalytic surface. A blind test at −75 °C (same amount of sample without Pd) showed an amount of adsorption CO—which is 4.3% of the sample—containing Pd, and this amount was subtracted from the total chemisorbed CO.

2.9. Kinetic Studies on ES-Pd/RGO/Al/c

Taking into account the environmental problems due to the widespread toluene emissions, within the present study, the case of toluene is selected for obtaining the reaction kinetics equations for further application in the design of catalytic reactors for abatement of VOCs in waste gases.

A reliable reactor design requires obtaining data on the behaviour of the catalyst at different reaction conditions. Therefore, as a further extension of the catalytic studies, the kinetics and the mechanism of the reaction of complete oxidation of toluene on ES-Pd/RGO/Al/c catalyst were carried out. In order to obtain data suitable for the kinetics calculations, the reaction temperature was kept almost constant (maximum deviation: ±1 °C). The isothermal operation of the reactor was approved by tests with reactions producing up to 45 °C adiabatic rise; the gradient of 2 °C was measured at conversion above 98% by thermocouples before and inside the catalytic bed (the possible “channeling” effect

was avoided by the mobile installation of the thermocouple in the catalytic bed). Therefore, for the present study, conversions below 40–45% were used. The reactor isothermal zone was measured to be 6.5 cm, which can be considered sufficient for the present catalyst volume. The pressure drop within the system was neglected (measured to be below 2 kPa). Preliminary measurements at GHSV above 40,000 h⁻¹ showed no significant differences in the values for the integrated reaction rate (first-order kinetics). The radial concentration profile and the axial dispersion effect were neglected because the catalyst bed represents a chain of more than 10 ideal-mixing cells; therefore, the geometrical characteristics and the flow conditions of the catalytic bed allow the consideration of the reactor to be close to the case of the isothermal plug flow reactor. On this basis, for the kinetics experiments, the gaseous hourly space velocity (GHSV_{STP}) was fixed at 100,000 h⁻¹. In order to minimize the internal diffusion effects, the experiments were performed at a supported catalyst particle size below 0.05 mm; thus, the calculated effectiveness factor (assuming first-order kinetics) showed values above 0.95 (conversions below 40–45%), and the limit was applied for calculation the kinetics parameters.

The kinetics parameters calculations were performed by varying the inlet concentrations of the reagents. The approach, described by Duprat [45], was applied for the kinetic parameters' estimation. The calculation procedure was previously described in detail [46]. For these calculations, data from the light-off curves were used and the kinetics parameters were derived using direct integration of the reaction rate. To fit the experimentally measured rates with kinetics parameters, a computation program for the material balance in an isothermal plug flow reactor and a numerical nonlinear optimization procedure were applied. The minimization of the residual sum of squares between the measured experimental points and the predictions of the model (RSS) and the square of the correlation coefficient (R²) were used as optimization quality criteria and model consistency.

A power-law kinetic model (PWL) was used as a first approximation for further selection among the applied mechanistic models. The obtained results are presented in Table 3.

Table 3. Kinetics parameters based on the power-law model.

	PWL						
	$r = k C_{voc}^m C_{ox}^n C_{water}^p$						
	E _a	k _o	m (C ₇ H ₈)	n (O ₂)	p (H ₂ O)	RSS	R ²
ES-Pd/RGO/Al/c	114.9 ± 1.7	(1.69 ± 0.03)10 ¹²	0.220 ± 0.003	0.490 ± 0.007	-0.03 ± -0.05 × 10 ⁻²	2.3	0.99

E_{ai}, kJ/mol; k_{oi}, mol·s⁻¹·m⁻³; k_{oi,pwl}, mol·s⁻¹·[1 - (m + n + p)]; E_{ai}, kJ/mol. (R²)—squared correlation coefficient.

The values for the observed reaction order towards the oxygen and toluene (0.2 and 0.5, respectively) lead to the suggestion of a significant role for chemisorption. The reaction order towards the water vapor shows a very weak inhibition effect (-0.03). The impact of the water vapor formed during the reaction and the oxygen consumption is taken into account during the integration of the reaction rate alongside the catalytic bed.

Direct and quantitative kinetic analysis of the reactivity of the tested compounds is limited due to the significant differences in the reaction temperatures. An alternative possibility is to apply the first-order kinetics calculations (E_{app}, k_o) and after averaging the E_{app}, to compare the pre-exponential factors. Subtracting the CO case (where the activation energy is 371 kJ/mol), for the rest VOCs, the values of E_{app} are within the limits of 113 kJ/mol (propylene) to 156 kJ/mol (butane), averaged E_{app} being 136 kJ/mol. Still, the described approach is not applicable due to the same reason: large temperature differences in S-curves from propylene to butane. An additional possibility is to compare the first-order rate constants at a fixed temperature, where it is possible for a group of S-curves. In this case, we have the following order of reactivity: propane: 1.0 (lowest, assumed as basis line); butane: 3.0; n-hexane: 11.4; dimethyl ether: 26.6. Further, analysing the reactivity of the part of the studied hydrocarbons (in the reaction of complete oxidation), one can see that it increases from propane to n-hexane, which shows some correlation with the

lowering of the dissociation energies of the weakest C-H bond within the corresponding hydrocarbon [43,44]. The proper values reported in [43] are: methane—439 kJ/mol, ethane—421 kJ/mol, propane—411 kJ/mol, n-butane—411 kJ/mol).

Based on the analysis of the PWL, several models were proposed for the description of the kinetics of the catalytic oxidation of toluene on the ES-Pd/RGO/Al/c catalyst: Mars–van Krevelen (MVK), Langmuir–Hinshelwood (LH), and Eley–Rideal (ER). The chosen models represent a general selection of as many as possible complex forms of the three main reaction mechanisms: (i) the oxidation proceeds by oxygen from the catalyst; (ii) reagents are reacting in their adsorbed forms without oxygen supply from the catalyst; and (iii) one of the reagents is reacting from the gas phase. It is worth mentioning that despite the fact that the values for the reaction orders towards toluene and oxygen are not close to unity, the Eley–Rideal mechanism (the direct reaction of toluene or oxygen from the gas phase, according to Equation (1)) cannot be entirely rejected.

$$r = \frac{kC_{voc}K_{voc}C_{ox}}{1 + K_{voc}C_{voc} + K_{water}C_{water}} \quad (1)$$

The inclusion of the adsorption effects is performed by the calculation of the expected heats of adsorption (ΔH_i) and the corresponding adsorption equilibrium constants ($K_{i(voc,ox)}$) within the applied mechanistic models (ER, LH, MVK). The calculation of the kinetics parameters is based on the following formulas' reaction rate constants: $k_i = k_{0,i}e^{-E_{a,i}/RT}$; k , k_{red} , k_{ox} (for power-law, Langmuir–Hinshelwood, and Eley–Rideal models and the reduction and oxidation steps of the reaction for the Mars–Van Krevelen mechanism, respectively); the adsorption equilibrium constants K_i ($i = O_2, VOC, H_2O$) are calculated from the ratio between the rates of adsorption and desorption, both of them being exponentially dependent on the temperature, which is depicted as follows: $k_{ads} = k_{0,ads}e^{-E_{ads}/RT}$; $k_{des} = k_{0,des}e^{-E_{des}/RT}$; thus, $K_i = \frac{k_{ads}}{k_{des}}$. The difference ($E_{ads} - E_{des}$) is the heat of adsorption ΔH . The specific dimensions of the kinetics parameters and the obtained results are presented in Table 4.

Table 4. Reaction rate expressions and kinetics parameters for applied ER, MVK, and LH models.

Parameters	Models		
	ER: Water Competes with Toluene	MVK: Water Adsorbs on Oxidized and Reduced Sites, Slow Desorption of Products	LH: Adsorption on Different Sites, Water Competes with Oxygen and Toluene
E_a	98.6 ± 1.5	n/a	122.2 ± 1.8
k_o	$(5.37 \pm 0.08) \times 10^{11}$	n/a	$(1.01 \pm 0.02) \times 10^{13}$
$-\Delta H_{voc}$	68.0 ± 1.0	n/a	61.5 ± 0.9
$k_{o,voc}$	$(1.56 \pm 0.02) \times 10^{-6}$	n/a	$(2.14 \pm 0.03) \times 10^{-4}$
$-\Delta H_{wat}$	51.2 ± 0.8	n/a	n/a
$k_{o,wat}$	$(2.30 \pm 0.03) \times 10^{-6}$	n/a	n/a
$E_{a,ox}$	n/a	132.4 ± 2.0	n/a
$k_{o,ox}$	n/a	$(3.73 \pm 0.06) \times 10^{14}$	$(7.76 \pm 0.12) \times 10^{-6}$
$E_{a,red}$	n/a	41.6 ± 0.62	n/a
$k_{o,red}$	n/a	$(8.42 \pm 0.13) \times 10^6$	n/a
$-\Delta H_{wat,ox}$	n/a	1.13 ± 0.02	51.0 ± 0.8
$k_{o,wat,ox}$	n/a	3.76 ± 0.06	$(1.10 \pm 0.02) \times 10^{-8}$
$-\Delta H_{wat,red}$	n/a	14.7 ± 0.2	43.2 ± 0.6
$k_{o,wat,red}$	n/a	$(1.93 \pm 0.03) \times 10^{-3}$	$(7.24 \pm 0.11) \times 10^{-5}$
$E_{a,des}$	n/a	46.0 ± 0.7	n/a
$-\Delta H_{ox}$	n/a	n/a	44.2 ± 0.7
RSS	6.4	10.7	2
R ²	0.98	0.99	0.99

E_{ai} , kJ/mol; ΔH_i , kJ/mol; k_{oi} , atm⁻¹; $k = k_o \cdot \exp(-E_a/RT)$; $K_{i(voc,ox)} = k_{o(voc,ox)} \cdot \exp(-\Delta H_{i,voc,ox}/RT)$; $-\Delta H_i = E_{des} - E_{ads}$, (R^2), squared correlation coefficient; n/a , not applicable. The Mars–Van Krevelen mechanism considers that the gaseous toluene is oxidized by the oxygen species originating from the lattice of the solid active phase [47]. The inhibiting effect of the water vapour (both produced by the reaction or additionally added to the gas feed) was accounted for by adding terms in the denominator connected to the water adsorption; thus, the original Mars–Van Krevelen model was modified [48]. In this study, the kinetic parameters obtained by the Mars–Van Krevelen model show that there is a competition between water molecules and toluene molecules for the oxidized and reduced catalytic sites, which also accounts for the effect of slow product desorption. Based on the analysis of the MVK model, one may conclude that there is a very fast reduction rate and slow re-oxidation stage ($r_{red} \gg r_{ox}$). The model calculations show that the water preferentially affects the oxidized sites ($k_{o,wat,red} \ll k_{o,wat,ox}$). An interesting idea for a variety of different MVK mechanisms, including accounting for two types of active sites, was presented in a state-of-the-art study, published earlier by Heynderickx et al. [49]. One may suggest that within the present MVK model, this interesting idea for two types of sites could be considered to be partly included in an implicit way. The simplified consideration assumes that the two types of active sites should be Pd and PdO, respectively. However, the complex character of the catalytic system required to be included also the influences the RGO: its role during the catalytic process' contact with the palladium particles, most likely played at the boundary regions, is still not clarified sufficiently in the literature. Thus, further extending the applied general mechanistic models, including by comparative data for TOF, will be of significant interest. The kinetic data, according to Equation (2), are presented in Table 4.

$$r = \frac{k_{red}k_{ox}C_{voc}C_{ox}}{\gamma k_{red}C_{voc}(1 + K_{water-voc}C_{water-voc}) + k_{ox}C_{ox}(1 + K_{water-ox}C_{water-ox}) + (k_{red}k_{ox}/k_{des})C_{voc}C_{ox}}, \gamma = 9 \quad (2)$$

Furthermore, the mechanistic model of Langmuir–Hinshelwood was applied, where the reaction proceeds between the reagents adsorbed on different types of active sites (Table 4). In this case, the oxygen from the active phase does not take part in the oxidation process. The water molecules formed as reaction products may compete with the molecules of toluene and oxygen for their preferential sites of adsorption. The reaction rate follows Equation (3).

$$r = \frac{kK_{voc}C_{voc}K_{ox}C_{ox}}{(1 + K_{voc}C_{voc} + K_{water-voc}C_{water-voc})(1 + K_{ox}C_{ox} + K_{water-ox}C_{water-ox})} \quad (3)$$

The relevance of the mechanistic models used for the kinetic calculations towards the experimental data set is presented in Figure 8, where the correlation between the measured and the predicted conversions by the power-law kinetics equation (PWL) and the applied mechanistic models (ER, MVK, and LH) is plotted. One can see from Figure 8 and Tables 3 and 4 that the lowest values for RSS criteria and the highest correlation between the model and experiment are obtained for the Langmuir–Hinshelwood model, which suggests that this mechanism is more consistent with the experimental results than the other mechanisms applied within the present study. In this case, the complete oxidation of toluene occurs on the solid surface of the catalyst from adsorbed toluene and oxygen that these species react to form the reaction products: carbon dioxide and water. It is worth mentioning that other authors have found that Langmuir–Hinshelwood is more appropriate for the catalytic oxidation of VOCs over the catalysts supported on carbon materials [35,50].

A two-dimensional model of a catalytic reactor was used for the simulation of the toluene combustion ((Figure 9). The calculated conversion and temperature profiles using the obtained data for the kinetics of the toluene combustion were used to evaluate the possibilities for abatement of toluene emissions at conditions close to the real practice (a

heat loss is predicted; therefore, it is more precise to define the reactor as semi-adiabatic). The results show that for treatment of $53,900 \text{ Nm}^3 \text{ h}^{-1}$ toluene containing waste gas (C_7H_8 : 0.03 vol.%, H_2O : 2.2 vol.%, O_2 : 16 vol.%), the needed catalyst amount for achieving 99.0% is 1.766 m^3 ($D = 3.0 \text{ m}$, $L = 0.25 \text{ m}$) (Figure 9). Figure 9 demonstrates the possibilities for high efficiency of the catalyst in cleaning model waste gases containing toluene at an inlet temperature below $190 \text{ }^\circ\text{C}$.

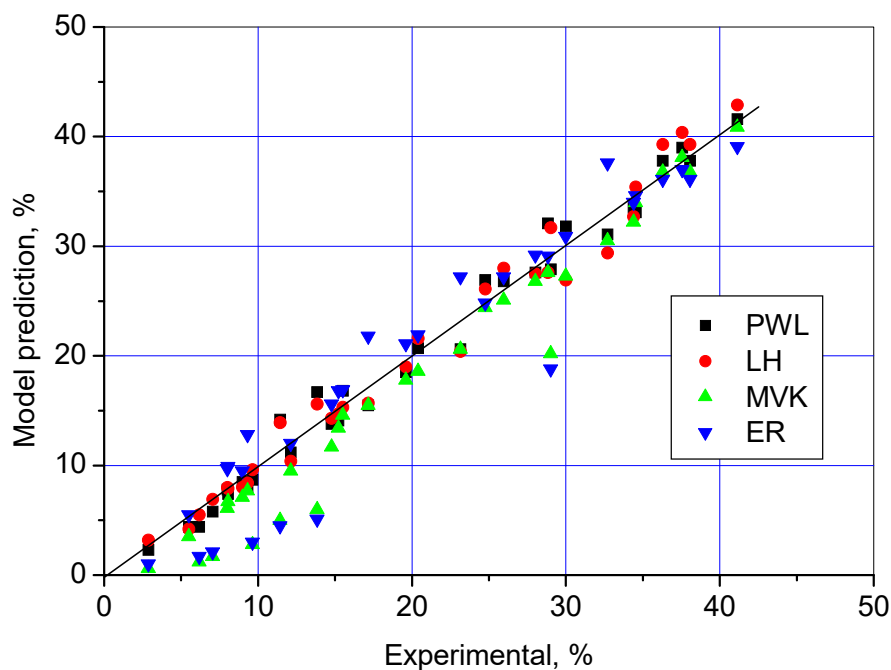


Figure 8. Correlation between the measured and the predicted conversions by the power-law kinetics equation (PWL) and the applied mechanistic models (ER, MVK and LH).

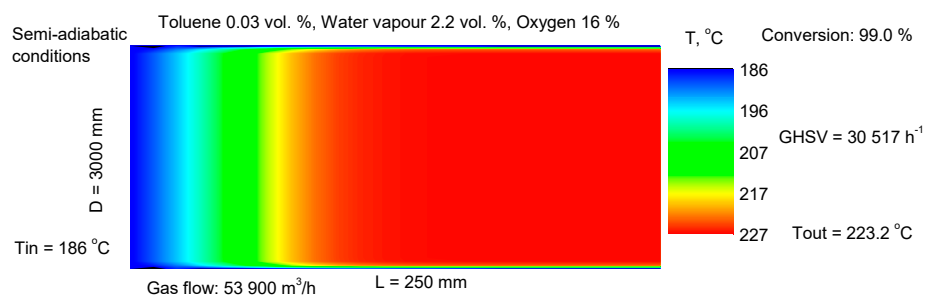


Figure 9. Reactor model for predicting the conditions for 99.0% conversion of 300 ppm toluene in waste gases at semi-adiabatic conditions.

There is no consensus in the literature on which form of palladium plays the main role in the oxidation reaction. Some papers argued that Pd^{2+} is more active than Pd^0 [51,52]; other authors claim the opposite [53]. Serious arguments that both forms participate in the oxidation of VOCs are also published [54]. The influence of palladium particle size is also discussed as an important factor for catalytic activity [35]. The long-term activity and stability of the conversion degree for this catalyst need some additional considerations concerning the transformation of the active phase during the catalytic reaction. According to the results from XRD, TEM, and XPS, the fresh ES-Pd/RGO/Al/c catalyst PdO is the predominant phase. In the course of the reaction, some PdO is reduced; thus, the quantity of Pd on the surface increases. However, it is believed that on the catalyst's surface, additional processes that may lead to re-oxidation of the palladium particles occur. It is well known that water and CO_2 molecules that evolved as products of VOCs oxidation reaction can dissociate on the surface to highly oxidative O^- species, which may react with Pd^0 to

form Pd²⁺ [55,56]. Due to the hydrophobic character of the RGO support, water molecules quickly detach from the surface, liberating active centres for the reagents' adsorption. Thus, the reaction rate remains high. Meanwhile, the re-oxidation process leads to the production of new small-size PdO particles, which retain the balance of the oxidation state of palladium.

3. Materials and Methods

3.1. Materials

The reduced graphene oxide (RGO) was obtained by the following procedure: 1 g powdered synthetic graphite (99% carbon, 50 mesh Sigma-Aldrich, Saint Louis, MO, USA) was poured in a mixture of 36 mL of H₂SO₄ and 4 mL of H₃PO₄ and stirred for 30 min in an ice bath. The following step was the drop-wise addition of 6 g of KMnO₄ and 100 mL of distilled water. Sonication for 15 min using a Sonix ultrasonic processor (20 KHz, 750 W) was applied in order to exfoliate the graphite sheets [57]. The final step was thorough washing of the obtained GO with deionized water. Part of the material was left as a suspension and for the rest, the reducer L-ascorbic acid was added to obtain RGO. The as-prepared RGO was dried at 90 °C for 12 h and thermally treated for 3 h at 600 °C in Ar flow.

The alumina gel was prepared using the sol–gel method from aluminium isopropoxide (99.9%, Sigma-Aldrich) hydrolysed by the procedure described in [58]. After dissolution, an appropriate amount of 1 M nitric acid was added. The slurry was kept under vigorous stirring at 100 °C and refluxed for 72 h. The Al content in the final product was 8–10 wt. %. The composite RGO-alumina (RGO–Al) was obtained hydrothermally from a mixture of 15 g of GO suspension (0.01395 g/mL) and 15 g of AlOOH gel at 160 °C for 15 h. After the synthesis, the composite was thermally treated at 475 °C for 3 h in air. Pd was loaded on it through the incipient wetness method using palladium acetate dissolved in acetone followed by heating at 420 °C for 40 min in air. The content of the loaded Pd was estimated to be 0.5 wt. %. This catalyst, designed for laboratory studies, is denoted further as Pd/RGO–Al.

The second type of catalyst (egg-shell-like (ES), designed for practical application) was prepared by loading Pd on the RGO using palladium acetate dissolved in acetone followed by heating at 420 °C for 40 min in air. This fine-powdered material was deposited on the surface of the ceramic carrier (c) using the aforementioned alumina gel as a binder (Al). The content of the loaded Pd was also estimated to be 0.5 wt. %. This catalyst is denoted further as ES-Pd/RGO/Al/c.

3.2. Characterization

Powder X-ray diffraction (XRD) patterns were recorded within the 5–90 2θ region on a Bruker D8-Advance Diffractometer (Karlsruhe, Germany) with CuK_α radiation and LynxEye detector. The phase identification was performed by the EVA software package using the ICDD-PDF-2(2021) database. Topas-4.2 program (Karlsruhe, Germany) [59] was used for Rietveld quantification and the mean coherent domain sizes' determination.

The morphology and elemental composition of the fresh catalysts were studied on a scanning electron microscope JEOL JSM-6390 (Tokyo, Japan) equipped with an energy dispersive spectroscopy (EDS) (Oxford Instruments, Oxford, UK).

The texture characteristics of the prepared materials were derived from the adsorption–desorption isotherms obtained by low-temperature N₂ adsorption at 77 K on the Quantachrome Nova 1200e instrument (Boynton Beach, FL, USA). The specific surface area was determined by the BET equation, the total pore volume was calculated at the end of the isotherm close p/p₀ ≈ 0.99, and the mean pore diameter was determined by NLDFT (slit pores, equilibrium model). The pore size distributions were made by NLDFT (slit pores, equilibrium model).

The XPS measurements were carried out on an AXIS Supra electron spectrometer (Kratos Analytical Ltd., Manchester, UK) using Al K_α radiation with a photon energy of

1486.6 eV. Prior to measurements, the catalysts were held in the ultra-high vacuum chamber for 16 h. The peak deconvolution was carried out using the commercial data-processing software (ESCAPE™ Kratos Analytical Ltd., Manchester, UK) considering a Shirley-type background and Gaussian–Lorentzian curve fitting.

Transmission electron microscopy (TEM) analyses were performed to reveal the morphology of the catalysts before and after the catalytic test. The instrument used was a JEOL JEM 2100 microscope (JEOL Ltd., Tokyo, Japan) at an accelerated voltage of 200 kV. Sample preparation included the dispersion of a small amount of powdered samples in ethanol followed by 3 min of sonication. A standard TEM copper grid covered with amorphous carbon was used as a sample carrier. The phase composition was evaluated by electron diffraction. High-resolution (HRTEM) images were also used for the determination of the phases in the samples.

The CO chemisorption tests were performed by pulse technique under the following conditions: carrier gas: 400 mL/min argon 5.0 with oxygen concentration below 1 ppm (measured by SGM7 gas analyser, Zirox, Greifswald, Germany); the volume of CO impulses: 1.50 cm³, injected by a four-port valve; a gas mixture containing 5 vol. CO in Ar (5.0); preliminary reduction of the samples at 340 °C for 3 h in 5 vol.% H₂/Ar (5.0); a temperature of CO chemisorption: −75 °C (maintained by dry ice) and 0 °C; mass-flow controllers Bronkhorst mod. El-flow; gas analysis by NDIR gas analyser Horiba VA3000 (Kyoto, Japan). The assumed stoichiometry is 1, i.e., one CO molecule adsorbs on one Pd-atom, the cross-sectional area of the active metal atom of Pd being 0.0787.10^{−18} m².

3.3. Catalytic Tests

The tests on complete catalytic oxidation of different VOC (propane, butane, hexane, dimethyl ether, toluene, propylene) and CO on Pd/RGO-Al catalyst were carried out in a fixed bed reactor with a gaseous hourly space velocity (GHSV_{STP}) of 100,000 h^{−1} and 30,000 h^{−1} for ES-Pd/RGO/Al/c catalyst, respectively. The catalyst amounts are the following: a catalyst in the form of the fraction: 0.30 cm³ (0.34 g); supported catalysts: 1.0 cm³ (1.83 g) for comparative activity tests: 0.5 cm³; (0.93 g catalyst and 0.91 g “blind” sample) for kinetics study and for CO chemisorption measurements.

The catalytic activity measurements were performed at the following inlet concentrations of the reagents: 170 ppm for propane, 100 ppm for butane, 170 ppm for hexane, 250 ppm for dimethyl ether, 150 ppm for toluene, 300 ppm for propylene, and 550 ppm for CO, and 9.5 vol.% O₂. All gaseous mixtures were balanced to 100% with nitrogen (4.6). The total catalyst bed volume was 1.0 cm³ and the reactor diameter was 6 mm. On-line gas analysers (CO, CO₂/O₂, Teledyne) and THC-FID (Thermo FID-TG, SK Elektronik GmbH) for analysis of total hydrocarbon content, equipped with a flame ionization detector, were applied for the converted gas mixture analysis. The long-term stability experiments were carried out at varied test conditions: first 100 h the samples were treated in the absence of water vapor where the activity was increasing gradually. After reaching stabilization, the stability test continued in the presence of 1% water vapor and the stabilization plateau was maintained for at least 200 h.

For obtaining data for reaction kinetics calculations, the inlet concentrations of reactants were varied as follows: toluene feed concentrations: 60, 142, and 225 ppm; feed oxygen on levels of 1.2, 5.1, 9.9, and 20.5 vol.%; additional water vapor on levels of 0, 0.55, 1.10, and 2.20 vol.%. All feed gas mixtures were balanced with nitrogen (4.0). The kinetics tests were carried out at GHSV_{STP} of 62,000 h^{−1}. The reproducibility and the confidence intervals for the measured conversion degrees were the subjects of preliminary tests, which consist of repeating the tests under similar but not identical conditions in separate experimental runs, presented in the study. The calculated value for the standard deviation (±1.5%) was based on the average of six measurements at each experimental point. The reported results are based on the average values for the conversion degree within two parallel measurements. The approach applied within the present study is based on the experimental establishment of the conditions when the effect of the external

mass transfer limitations is minimized. It consists of the calculation of the reaction rate (integrated alongside the reactor in an axial direction) up to reaching a constant value, while gradually increasing the GHSV. In parallel, comparative calculations are performed regarding the changes in the mass transfer coefficient (ranging from 0.06 to 0.11 m/s), with the gas flow being varied.

3.4. Reactor Model for Simulation of the Process of Toluene Abatement in Waste Gases

A two-dimensional model of a catalytic reactor was used for simulation of the toluene combustion at conditions close to the practice. Detailed descriptions on the principles and the applied calculation procedures are given in the literature [60,61]. The heat transfer within the catalyst bed in the radial and axial direction is based on the relation between the effective radial dispersion coefficient E_r and the thermal conductivity λ_r , given as follows:

$$E_r = \frac{\lambda_r}{\rho C_p} \quad (4)$$

The wall boundary condition has the following expression:
 $r = R$ (wall):

$$-\lambda_r \frac{\partial T}{\partial r} = h_r (T_R - T_{wall}) \quad (5)$$

where h_r is the heat transfer coefficient, whose value can be found in an empirical way.

The temperature and concentration profiles are calculated by the following set of equations:

$$u_r \frac{\partial T}{\partial z} = E_r \left(\frac{\partial^2 T}{\partial r^2} + \frac{1}{r} \frac{\partial T}{\partial r} \right) - \frac{\Delta H_R R_{(C,T)}}{\rho C_p} \quad (6)$$

$$u_r \frac{\partial C_g}{\partial z} = D_r \left(\frac{\partial^2 C_g}{\partial r^2} + \frac{1}{r} \frac{\partial C_g}{\partial r} \right) + R_{(C,T)} \quad (7)$$

A second-order approximation is applied for the numerical solution of the equations. The conversion at the outlet of the reactor was calculated using the method of mixing-cup average concentration.

4. Conclusions

A highly active, novel, complex catalyst with an innovative design for complete oxidation of VOCs has been successfully prepared using a composite active phase of Pd-nanoparticles with RGO loaded as an “egg-shell” on ceramic support via an alumina hydrogel binder. Due to the specific interaction between the catalyst’s constituents, the new formulation of the active phase is able to completely oxidize VOCs (toluene, propylene, propane, butane, hexane, dimethyl ether) and CO at low temperatures (100–350 °C). The very significant advantage of the catalyst is the weak effect of water vapor on the catalytic activity (reaction order towards the water vapor during toluene combustion is -0.03). Using a variety of instrumental methods (XRD, TEM, and XPS), it was established that for high activity (efficiency) and long-term stability, the optimal ratio Pd/PdO is close to 1:1. It was established that the reaction of complete toluene oxidation most likely proceeds via the mechanism of Langmuir–Hinshelwood. The results obtained lead to further perspectives for the application of the currently developed approach for the preparation of large-scale monolithic catalytic systems for air pollution control.

Supplementary Materials: The following supporting information can be downloaded at: <https://www.mdpi.com/article/10.3390/catal13081224/s1>, Figure S1: CO chemisorption on ES-Pd/RGO/Al/c [47].

Author Contributions: Conceptualization, D.K. (Daniela Kovacheva) and I.S.; methodology, D.K. (Daniela Kovacheva) and I.S.; formal analysis, D.K. (Diana Kichukova), D.K. (Daniela Kovacheva), I.S., R.V., V.T. and G.A.; investigation, D.K. (Daniela Kovacheva), A.N. and I.S.; data curation, D.K. (Diana Kichukova), V.T.; writing—original draft preparation, D.K. (Daniela Kovacheva), A.N. and I.S.; writing—review and editing, D.K. (Daniela Kovacheva), A.N., R.V. and I.S.; visualization, D.K. (Daniela Kovacheva), I.S., R.V., A.N. and G.A.; project administration, I.S. All authors have read and agreed to the published version of the manuscript.

Funding: This research was funded by the National Science Fund, Project KP-06-H 59/8.

Data Availability Statement: Not available.

Acknowledgments: Research equipment of distributed research infrastructure INFRAMAT (part of Bulgarian National roadmap for research infrastructures) supported by Bulgarian Ministry of Education and Science under contract D01-172/28.07.2022 were used in this investigation.

Conflicts of Interest: The authors declare no conflict of interest.

Nomenclature

C_g	concentration of toluene at working conditions, mol/m ³ ;
D_r	radial diffusion coefficient, m ² /s;
E_r	effective radial dispersion coefficient for heat, m ² /s;
ΔH_r	heat of reaction, J/mol;
C_p	specific heat capacity, J/K.kg;
u_r	gas velocity at radial coordinate r, m/s;
$R_{(C,T)}$	reaction rate, mol/m ³ .s;
r	radial coordinate, m;
z	axial coordinate, m;
λ_r	effective radial thermal conductivity, W/m.K;
ρ	gas density, kg/m ³ .

References

1. Finlayson-Pitts, B.J.; Pitts, N.J. Tropospheric air pollution: Ozone, airborne toxics, polycyclic aromatic hydrocarbons, and particles. *Science* **1997**, *276*, 1045–1051. [\[CrossRef\]](#)
2. Iranpour, R.; Cox, H.H.J.; Deshusses, M.A.; Schroeder, E.D. Literature review of air pollution control biofilters and biotrickling filters for odor and volatile organic compound removal. *Environ. Prog.* **2005**, *24*, 254–267. [\[CrossRef\]](#)
3. Tomatis, M.; Xu, H.-H.; He, J.; Zhang, X.-D. Recent development of catalysts for removal of volatile organic compounds in flue gas by combustion: A review. *J. Chem.* **2016**, *2016*, 8324826. [\[CrossRef\]](#)
4. Vu, V.H.; Belkouch, J.; Ould-Driss, A.; Taouk, B. Removal of hazardous chlorinated VOCs over Mn-Cu mixed oxide based catalyst. *J. Hazard Mater.* **2009**, *169*, 758–765. [\[CrossRef\]](#) [\[PubMed\]](#)
5. Zhang, Z.; Jiang, Z.; Shangguan, W. Low-temperature catalysis for VOCs removal in technology and application: A state-of-the-art review. *Catal. Today.* **2016**, *264*, 270–278. [\[CrossRef\]](#)
6. He, C.; Cheng, L.; Zhang, X.; Douthwaite, M.; Pattison, S.; Hao, Z. Recent Advances in the Catalytic Oxidation of Volatile Organic Compounds: A Review Based on Pollutant Sorts and Sources. *Chem. Rev.* **2019**, *119*, 4471–4568. [\[CrossRef\]](#) [\[PubMed\]](#)
7. Song, S.; Zhang, S.; Zhang, X.; Verma, P.; Wen, M. Advances in Catalytic Oxidation of Volatile Organic Compounds over Pd-Supported Catalysts: Recent Trends and Challenges. *Front. Mater.* **2020**, *7*, 595667. [\[CrossRef\]](#)
8. Liotta, L.F. Catalytic oxidation of volatile organic compounds on supported noble metals. *Appl. Catal. B Environ.* **2010**, *100*, 403–412. [\[CrossRef\]](#)
9. Fu, Z.; Liu, L.; Song, Y.; Ye, Q.; Cheng, S.; Kang, T.; Dai, H. Catalytic oxidation of carbon monoxide, toluene, and ethyl acetate over the xPd/OMS-2 catalysts: Effect of Pd loading. *Front. Chem. Sci. Eng.* **2017**, *11*, 185–196. [\[CrossRef\]](#)
10. Liu, R.; Wu, H.; Shi, J.; Xu, X.; Zhao, D.; Ng, Y.H.; Zhang, M.; Liu, S.; Ding, H. Recent progress on catalysts for catalytic oxidation of volatile organic compounds: A review. *Catal. Sci. Technol.* **2022**, *12*, 6945–6991. [\[CrossRef\]](#)
11. Liu, Y.; Deng, J.; Xie, S.; Wang, Z.; Dai, H. Catalytic removal of volatile organic compounds using ordered porous transition metal oxide and supported noble metal catalysts. *Chin. J. Catal.* **2016**, *37*, 1193–1205. [\[CrossRef\]](#)
12. Tian, Z.-Y.; Ngamou, P.H.T.; Vannier, V.; Kohse-Höinghaus, K.; Bahlawane, N. Catalytic oxidation of VOCs over mixed Co–Mn oxides. *Appl. Catal. B Environ.* **2012**, *117–118*, 125–134. [\[CrossRef\]](#)
13. Kamal, M.S.; Razzak, S.A.; Hossain, M.M. Catalytic oxidation of volatile organic compounds (VOCs)-a review. *Atmos. Environ.* **2016**, *140*, 117–134. [\[CrossRef\]](#)

14. Xiong, H.F.; Wiebenga, M.H.; Carrillo, C.; Gaudet, J.R.; Pham, H.N.; Kunwar, D.; Oh, S.H.; Qi, G.; Kim, C.H.; Datye, A.K. Design considerations for low-temperature hydrocarbon oxidation reactions on Pd based catalysts. *Appl. Catal. B Environ.* **2018**, *236*, 436–444. [[CrossRef](#)]
15. Odoom-Wubah, T.; Li, Q.; Adilov, I.; Huang, J.; Li, Q. Towards efficient Pd/Mn₃O₄ catalyst with enhanced acidic sites and low temperature reducibility for benzene abatement. *Mol. Catal.* **2019**, *477*, 110558. [[CrossRef](#)]
16. Bendahou, K.; Cherif, L.; Siffert, S.; Tidahy, H.L.; Benaïssa, H.; Aboukaïs, A. The effect of the use of lanthanum-doped mesoporous SBA-15 on the performance of Pt/SBA-15 and Pd/SBA-15 catalysts for total oxidation of toluene. *Appl. Catal. Gen.* **2008**, *351*, 82–87. [[CrossRef](#)]
17. González-Velasco, J.R.; Aranzabal, A.; López-Fonseca, R.; Ferret, R.; González-Marcos, J.A. Enhancement of the catalytic oxidation of hydrogen-lean chlorinated VOCs in the presence of hydrogen-supplying compounds. *Appl. Catal. B Environ.* **2000**, *33*, 24–43. [[CrossRef](#)]
18. Papaefthimiou, P.; Ioannides, T.; Verykios, X.E. Combustion of non-halogenated volatile organic compounds over group VIII metal catalysts. *Appl. Catal. B Environ.* **1997**, *13*, 175–184. [[CrossRef](#)]
19. Kim, S.C.; Shim, W.G. Properties and performance of Pd based catalysts for catalytic oxidation of volatile organic compounds. *Appl. Catal. B Environ.* **2009**, *92*, 429–436. [[CrossRef](#)]
20. Morales-Torres, S.; Maldonado-Hodar, F.J.; Perez-Cadenas, A.F.; Carrasco-Marín, F. Design of low-temperature Pt-carbon combustion catalysts for VOC's treatments. *J. Hazard. Mater.* **2010**, *183*, 814–822. [[CrossRef](#)]
21. Bell, A.T. The impact of nanoscience on heterogeneous catalysis. *Science* **2003**, *299*, 1688–1691. [[CrossRef](#)]
22. Baylet, A.; Royer, S.; Marécot, P.; Tatibouët, J.M.; Duprez, D. Effect of Pd precursor salt on the activity and stability of Pd-doped hexaaluminate catalysts for the CH₄ catalytic combustion. *Appl. Catal. B Environ.* **2008**, *81*, 88–96. [[CrossRef](#)]
23. Mojet, B.L.; Miller, J.T.; Ramaker, D.E.; Koningsberger, D.C. A New Model Describing the Metal–Support Interaction in Noble Metal Catalysts. *J. Catal.* **1999**, *186*, 373–386. [[CrossRef](#)]
24. Stakheev, A.Y.; Kustov, L.M. Effects of the support on the morphology and electronic properties of supported metal clusters: Modern concepts and progress in 1990s. *Appl. Catal. A Gen.* **1999**, *188*, 3–35. [[CrossRef](#)]
25. Gelin, P.; Primet, M. Complete oxidation of methane at low temperature over noble metal based catalysts: A review. *Appl. Catal. B Environ.* **2002**, *39*, 1–39. [[CrossRef](#)]
26. Mowery, D.L.; Graboski, M.S.; Ohno, T.R.; McCormick, R.L. Deactivation of PdO–Al₂O₃ oxidation catalyst in lean-burn natural gas engine exhaust: Aged catalyst characterization and studies of poisoning by H₂O and SO₂. *Appl. Catal. B Environ.* **1999**, *21*, 157–169. [[CrossRef](#)]
27. Ruiz, J.A.C.; Fraga, M.A.; Pastore, H.O. Methane combustion over Pd supported on MCM-41. *Appl. Catal. B Environ.* **2007**, *76*, 115–122. [[CrossRef](#)]
28. Ciuparu, D.; Lyubovsky, M.R.; Altman, E.; Pfefferle, L.D.; Datye, A. Catalytic combustion of methane over palladium-based catalysts. *Catal. Rev.* **2002**, *44*, 593–649. [[CrossRef](#)]
29. Persson, K.; Pfefferle, L.D.; Schwartz, W.; Ersson, A.; Jaras, S.G. Stability of palladium based catalysts during catalytic combustion of methane: The influence of water. *Appl. Catal. B Environ.* **2007**, *74*, 242–250. [[CrossRef](#)]
30. Groppi, G. Combustion of CH₄ over a PdO/ZrO₂ catalyst: An example of kinetic study under severe conditions. *Catal. Today* **2003**, *77*, 335–346. [[CrossRef](#)]
31. Chuang, K.T.; Zhou, B.; Tong, S. Kinetics and Mechanism of Catalytic Oxidation of Formaldehyde over Hydrophobic Catalysts. *Ind. Eng. Chem. Res.* **1994**, *33*, 1680–1686. [[CrossRef](#)]
32. Araya, P.; Guerrero, S.; Robertson, J.; Gracia, F.J. Methane combustion over Pd/SiO₂ catalysts with different degrees of hydrophobicity. *Appl. Catal. Gen.* **2005**, *283*, 225–233. [[CrossRef](#)]
33. Sharma, R.K.; Zhou, B.; Tong, S.; Chuang, K.T. Catalytic Destruction of Volatile Organic Compounds Using Supported Platinum and Palladium Hydrophobic Catalysts. *Ind. Eng. Chem. Res.* **1995**, *34*, 4310–4317. [[CrossRef](#)]
34. Wu, J.C.S.; Lin, Z.A.; Tsai, F.M.; Pan, J.W. Low-temperature complete oxidation of BTX on Pt/activated carbon catalysts. *Catal. Today* **2000**, *63*, 419–426. [[CrossRef](#)]
35. Bedia, J.; Rosas, J.M.; Rodríguez-Mirasol, J.; Cordero, T. Pd supported on mesoporous activated carbons with high oxidation resistance as catalysts for toluene oxidation. *Appl. Catal. B Environ.* **2010**, *94*, 8–18. [[CrossRef](#)]
36. Morales-Torres, S.; Perez-Cadenas, A.F.; Kapteijn, F.; Carrasco-Marín, F.; Maldonado-Hodar, F.J.; Moulijn, J.A. Palladium and platinum catalysts supported on carbon nanofiber coated monoliths for low-temperature combustion of BTX. *Appl. Catal. B Environ.* **2009**, *89*, 411–419. [[CrossRef](#)]
37. Wu, J.C.S.; Chang, T.Y. VOC deep oxidation over Pt catalysts using hydrophobic supports. *Catal. Today* **1998**, *44*, 111–118. [[CrossRef](#)]
38. Thommes, M.; Kaneko, K.; Neimark, A.; Olivier, J.P.; Rodríguez-Reinoso, F.; Rouquerol, J.; Sing, K.S.W. Physisorption of gases, with special reference to the evaluation of surface area and pore size distribution (IUPAC Technical Report). *Pure Appl. Chem.* **2015**, *87*, 1051–1069. [[CrossRef](#)]
39. De Pedro, Z.M.; Gomez-Sainero, L.M.; Gonzalez-Serrano, E.; Rodriguez, J.J. Gas-Phase Hydrodechlorination of Dichloromethane at Low Concentrations with Palladium/Carbon Catalysts. *Ind. Eng. Chem. Res.* **2006**, *45*, 7760–7766. [[CrossRef](#)]

40. Radkevich, V.Z.; Senko, T.L.; Wilson, K.; Grishenko, L.M.; Zaderko, A.N.; Diyuk, V.Y. The influence of surface functionalization of activated carbon on palladium dispersion and catalytic activity in hydrogen oxidation. *Appl. Catal. A* **2008**, *335*, 241–251. [[CrossRef](#)]
41. Moulder, J.F.; Stickle, W.F.; Sobol, P.E.; Bomben, K.D. *Handbook of X-ray Photoelectron Spectroscopy*; Chastain, J., King, R.C., Jr., Eds.; Physical Electronics, Inc.: Eden Prairie, MN, USA, 1995.
42. Kim, S.C. The catalytic oxidation of aromatic hydrocarbons over supported metal oxide. *J. Hazard. Mater.* **2002**, *91*, 285–299. [[CrossRef](#)] [[PubMed](#)]
43. Zboray, M.; Bell, A.T.; Iglesia, E. Role of C-H bond strength in the rate and selectivity of oxidative dehydrogenation of alkanes. *J. Phys. Chem. C* **2009**, *113*, 12380–12386. [[CrossRef](#)]
44. Deshlahra, P.; Iglesia, E. Reactivity and selectivity descriptors for the activation of C-H bonds in hydrocarbons and oxygenates on metal oxides. *J. Phys. Chem. C* **2016**, *120*, 16741–16760. [[CrossRef](#)]
45. Duprat, F. Light-off curve of catalytic reaction and kinetics. *Chem. Eng. Sci.* **2002**, *57*, 901–911. [[CrossRef](#)]
46. Markova-Velichkova, M.; Lazarova, T.; Tumbalev, V.; Ivanov, G.; Kovacheva, D.; Stefanov, P.; Naydenov, A. Complete oxidation of hydrocarbons on YFeO₃ and LaFeO₃ catalysts. *Chem. Eng. J.* **2013**, *231*, 236–244. [[CrossRef](#)]
47. Mars, P.; van Krevelen, D.W. Oxidations carried out by means of vanadium oxide catalysts. *Spec. Suppl. Chem. Eng. Sci.* **1954**, *3*, 41–59. [[CrossRef](#)]
48. Hurtado, P.; Ordóñez, S.; Sastre, H.; Diez, F.V. Development of a kinetic model for the oxidation of methane over Pd/Al₂O₃ at dry and wet conditions. *Appl. Catal. B Environ.* **2004**, *51*, 229–238. [[CrossRef](#)]
49. Heynderickx, P.; Thybaut, J.; Poelman, H.; Poelman, D.; Marin, G. Kinetic modeling of the total oxidation of propane over anatase and vanadia sputter deposited catalysts. *Appl. Catal. B Environ.* **2009**, *90*, 295–306. [[CrossRef](#)]
50. Trung, B.C.; Tu, L.N.Q.; Tri, N.T.M.; An, N.T.; Long, N.Q. Granular-carbon supported nano noble-metal (Au, Pd, Au-Pd): New dual-functional adsorbent/catalysts for effective removal of toluene at low-temperature and humid condition. *Environ Technol.* **2021**, *42*, 1772–1786. [[CrossRef](#)]
51. Yazawa, Y.; Yoshida, H.; Takagi, N.; Komai, S.; Satsuma, A.; Hattori, T. Oxidation state of palladium as a factor controlling catalytic activity of Pd/SiO₂-Al₂O₃ in propane combustion. *Appl. Catal. B Environ.* **1998**, *19*, 261–266. [[CrossRef](#)]
52. Burch, R.; Loader, P.K.; Urbano, F.J. Some aspects of hydrocarbon activation on platinum group metal combustion catalysts. *Catal. Today* **1996**, *27*, 243–248. [[CrossRef](#)]
53. Kim, S.C.; Nahm, S.W.; Shim, W.G.; Lee, J.W.; Moon, H. Influence of physicochemical treatments on spent palladium based catalyst for catalytic oxidation of VOCs. *J. Hazard. Mater.* **2007**, *141*, 305–314. [[CrossRef](#)] [[PubMed](#)]
54. Velinova, R.; Todorova, S.; Drenchev, B.; Ivanov, G.; Shipochka, M.; Markov, P.; Nihtianova, D.; Kovacheva, D.; Larin, A.V.; Naydenov, A. Complex study of the activity, stability and sulfur resistance of Pd/La₂O₃-CeO₂-Al₂O₃ system as monolithic catalyst for abatement of methane. *Chem. Eng. J.* **2019**, *368*, 865–876. [[CrossRef](#)]
55. Dury, F.; Gaigneaux, E.M.; Ruiz, P. The active role of CO₂ at low temperature in oxidation processes: The case of the oxidative dehydrogenation of propane on NiMoO₄ catalysts. *Appl. Catal. A* **2003**, *242*, 187–203. [[CrossRef](#)]
56. Demoulin, O.; Navez, M.; Mugabo, J.-L.; Ruiz, P. The oxidizing role of CO₂ at mild temperature on ceria-based catalysts. *Appl. Catal. B Environ.* **2007**, *70*, 284–293. [[CrossRef](#)]
57. Marcano, D.C.; Kosynkin, D.V.; Berlin, J.M.; Sinitskii, A.; Sun, Z.; Slesarev, A.; Alemany, L.B.; Lu, W.; Tour, J.M. Improved synthesis of graphene oxide. *ACS Nano* **2010**, *4*, 4806–4814. [[CrossRef](#)] [[PubMed](#)]
58. Yoldas, B.E. Alumina gels that form porous transparent Al₂O₃. *J. Mater. Sci.* **1975**, *10*, 1856–1860. [[CrossRef](#)]
59. Bruker, A.X.S. *TOPAS V4: General Profile and Structure Analysis Software for Powder Diffraction Data—User's Manual*; Bruker AXS: Karlsruhe, Germany, 2008. Available online: <http://algol.fis.uc.pt/jap/TOPAS%204-2%20Users%20Manual.pdf> (accessed on 7 July 2023).
60. Belfiore, L.A. *Transport Phenomena for Chemical Reactor Design*; John Wiley & Sons, Inc.: Hoboken, NJ, USA, 2003.
61. Nauman, E.B. *Chemical Reactor Design, Optimization, and Scaleup*; McGraw-Hill Companies: New York, NY, USA, 2002.

Disclaimer/Publisher's Note: The statements, opinions and data contained in all publications are solely those of the individual author(s) and contributor(s) and not of MDPI and/or the editor(s). MDPI and/or the editor(s) disclaim responsibility for any injury to people or property resulting from any ideas, methods, instructions or products referred to in the content.